

The ataxin-1 interactome reveals direct connection with multiple disrupted nuclear transport pathways

Sunyuan Zhang¹, Nicholas A. Williamson², David A. Jans³, and Marie A. Bogoyevitch^{1,*}

¹Cell Signalling Research Laboratories, Department of Biochemistry and Molecular Biology, and ²Bio21 Molecular Science and Biotechnology Institute, University of Melbourne, Parkville, Victoria 3010, Australia

³Nuclear Signalling Lab., Department of Biochemistry and Molecular Biology, Monash University, Clayton, Victoria 3800, Australia

* corresponding author: marieb@unimelb.edu.au

Summary (145 words)

The expanded polyglutamine (polyQ) tract form of ataxin-1 drives disease progression in spinocerebellar ataxia type 1 (SCA1). Although polyQ-ataxin-1 is known to form distinctive intranuclear bodies, the cellular pathways and functions it influences remain poorly understood. Here, we identify direct and proximal partners constituting the interactome of ataxin-1[85Q] in Neuro-2a cells. Pathways analyses indicate a significant enrichment of essential nuclear transporters in the interactome, pointing to disruptions in nuclear transport processes in the presence of polyQ-ataxin-1. Our direct assessments of nuclear transporters and their cargoes reinforce these observations, revealing disrupted trafficking often with relocalisation of transporters and/or cargoes to ataxin-1[85Q] nuclear bodies. Strikingly, the nucleoporin Nup98, dependent on its GLFG repeats, is recruited into polyQ-ataxin-1 nuclear bodies. Our results highlight a disruption of multiple essential nuclear protein trafficking pathways by polyQ-ataxin-1, a key contribution to furthering understanding of pathogenic mechanisms initiated by polyQ tract proteins.

Introduction

Spinocerebellar ataxia type 1 (SCA1) is an autosomal dominant neurodegenerative disease, associated with disabilities in coordination and movement and a marked atrophy in the cerebellum and brainstem¹. The genetic cause underlying SCA1 has been mapped to *ATXN1*, the gene encoding the ataxin-1 protein, whereby the CAG nucleotide repeat region of *ATXN1* is expanded in SCA1 patients². The resulting polyglutamine (polyQ) tract form of the ataxin-1 protein, polyQ-ataxin-1, forms distinctive nuclear bodies in individuals with SCA1, a feature recapitulated in SCA1 transgenic mice³. More broadly, polyQ tract expansions in specific proteins are now appreciated to drive at least 10 diseases⁴, and their study is providing exciting new insights that extend beyond critical aspects of protein biochemistry including protein folding/misfolding and protein-protein interactions to important points of regulation in cellular homeostasis dictated by proteostasis and impacts on cell survival/death-decision making^{5, 6, 7, 8, 9, 10, 11, 12}.

Several studies have reported disruptions in nuclear import/export processes in neurodegenerative diseases such as amyotrophic lateral sclerosis (ALS) and Huntington's disease (HD)^{13, 14, 15, 16}. The nuclear transport machinery responsible for the regulated

trafficking of proteins between the cytoplasm and the nucleus has a number of key components: nuclear import/export signals (NLS/NES) of the cargo proteins that direct their nuclear/cytoplasmic distributions, dedicated transport proteins responsible for nuclear import (importins) and export (exportins), the nuclear pore complex that spans the nuclear envelope and provides a regulated gateway for nuclear trafficking events, and the RanGTP/RanGDP system that drives directionality of the transport events^{17, 18}. Disrupting any of these entities can influence nucleocytoplasmic trafficking^{19, 20, 21}, making each of these a potential player in altered nuclear trafficking in neurodegenerative disease.

Here we approach the issues of the actions of polyQ-ataxin-1 from the perspective of protein-interaction networks, by first defining the interactome of ataxin-1[85Q]. By combining direct interaction analyses with our identification of polyQ-ataxin-1 proximal partners and pathways analyses, we not only confirm several known ataxin-1 interacting partners but we identify the nuclear transport pathway as the top-ranked cellular process defined by these interactors. By sequestering additional proteins into ataxin-1 nuclear bodies, polyQ-ataxin-1 has the potential to disrupt cellular homeostasis^{22, 23, 24}. To assess this possibility of ataxin-1 driven nuclear transport disruption, we define the relocation of multiple components of the nuclear transport machinery, often with their redistribution to ataxin-1[85Q] nuclear bodies. Our results reinforce a direct sequestration model for the impact of polyQ-ataxin-1 nuclear bodies.

Results and Discussion

Ataxin-1[85Q] forms distinctive nuclear bodies that are enhanced by arsenite stress

To define the suitability of the polyQ-ataxin-1 constructs GFP-ataxin-1[85Q] and MBI-ataxin-1[85Q] for interactome analyses in Neuro-2a cells, we assessed the subcellular localization of these proteins, compared to GFP or MBI alone, under control conditions and further in response to the pro-oxidant stressor arsenite^{25, 26}. Whilst GFP remains broadly distributed throughout the cell, GFP-ataxin-1[85Q] forms distinctive nuclear bodies that have been reported across a range of cell types^{22, 27, 28}; these GFP-ataxin-1[85Q] nuclear bodies formed within 24 h of transfection and increased in size upon acute arsenite exposure (300 μ M, 1 h) further highlighting their responsiveness to altered environmental conditions (Figure 1A).

Proximity biotinylation as driven by BirA* biotin ligase provides an alternative proteomics strategy for proximal partner identification²⁹. MBI-ataxin-1[85Q], the myc-tagged BirA* N-

terminal fusion with ataxin-1[85Q], was thus validated as per our workflow (Figure 1B). In contrast to MBI alone that was primarily cytoplasmic, MBI-ataxin-1[85Q] was largely restricted to the nucleus (Figure 1C). Streptavidin-based detection further confirmed widespread biotinylation by MBI alone whereas MBI-ataxin-1[85Q]-driven biotinylation was largely localised to prominent nuclear bodies (Figure 1C) with a restricted biotinylation profile as defined by streptavidin-detection of biotinylated proteins separated by SDS-PAGE (Figure 1D). Thus, we confirmed the formation of distinctive nuclear bodies by GFP-ataxin-1[85Q] or MBI-ataxin-1[85Q] and the suitability of these proteins for more detailed analyses of the polyQ-ataxin-1 interactome.

Complementary proteomics approaches identify nuclear transport proteins in the polyQ-ataxin-1 interactome

In subsequent analyses, we combined the power of BioID and Pulldown protocols as alternative and complementary approaches for interactome analyses³⁰ using both MBI-ataxin-1[85Q] and GFP-ataxin-1[85Q] in Neuro-2a cells under control and arsenite stress conditions (Figure 2A). Following trypsin-digestion of the proteins captured in the two different isolation protocols, our mass spectrometry and peptide raw data analysis defined the proteins present in each individual sample (Figure 2B). From the samples analysed as biological triplicates across the 4 conditions (BioID \pm arsenite, Pulldown \pm arsenite), and with the removal of non-specific proteins identified (see Methods), we recorded a total of 675 proteins (Supplementary Table S1), extending the breadth of the interactome of polyQ-ataxin-1, as previously investigated in non-neuronal (HEK293T) cell lysates co-immunoprecipitated with myc-ataxin-1³¹. Of note, we identified ataxin-1 itself, as well the well-characterised ataxin-1 partner protein Capicua transcriptional repressor (CIC)^{5, 32, 33, 34} under all 4 conditions, supporting the robustness of our approaches.

Of the 675 proteins of the ataxin-1 interactome, 91 were observed in at least 3 out of 4 of the conditions analysed (Figure 2B & C), Ingenuity Pathway Analysis revealing the top-ranked pathway to be Ran signaling (Figure 2D; see summary in Supplementary Table S2). Previous studies have reported the ALS-causing C9orf72 repeat expansion RNA product to interact directly with the Ran regulator Ran GTPase activating protein 1 (RanGAP1), resulting in its mislocalization and disruption of nucleocytoplasmic transport¹⁴. Significantly, RanGAP1, as well as the NPC component nucleoporin NUP62, colocalize with huntingtin protein aggregates

¹⁶, prompting us to examine the potential impact of polyQ-ataxin-1 on nuclear transport processes.

Classical nuclear transport pathways are disrupted by polyQ-ataxin-1

To begin to define the impact of polyQ-ataxin-1 on nuclear transport, we first examined well-characterised members of the importin (IMP) superfamily of nuclear transporters, importin- α 2 (IMP α 2), importin- β 1 (IMP β 1) and exportin-1 (also known as CRM1). In classical nuclear protein import, IMP β 1 mediates the transfer of cargo proteins across the nuclear pore complex either directly or in conjunction with IMP α 2 that acts as the adaptor binding both the cargo protein's NLS and IMP β 1 ¹⁹. When bound to RanGTP, CRM1 specifically recognises leucine-rich NESs to mediate protein export from the nucleus ³⁵. We coexpressed ataxin-1[85Q] with GFP-IMP α 2, -IMP β 1, -CRM1, or GFP alone as a control to assess the effect of ataxin-1[85Q] on nucleocytoplasmic distribution under either control or arsenite stress conditions (Figure 3). In the presence or absence of arsenite, GFP-IMP α 2 was primarily nuclear, as previously observed ³⁶, while GFP-IMP β 1 and -CRM1 were primarily cytoplasmic with a distinctive nuclear rim ^{37, 38}; GFP was distributed throughout the cytoplasm and nucleus. In the presence of ataxin-1[85Q], however, GFP-IMP α 2, -IMP β 1 and -CRM1 all showed prominent nuclear co-localisation with ataxin-1[85Q] that was further observed as striking nuclear bodies following arsenite stress exposure (Figure 3A-C, denoted by arrowheads in Zoom panels); no pronounced nuclear body distribution was observed for GFP alone (Figure 3D).

Mislocalisation of nuclear transporters would be expected to result in altered nucleocytoplasmic distribution of specific cargo proteins. Accordingly, we tested the impact of ataxin-1[85Q] expression on the nuclear accumulation of a classical importin α/β 1-recognised model cargo, GFP-NLS- β gal, containing the NLS from simian virus SV40 large tumour antigen (Figure 4). We observed prominent nuclear localization of GFP-NLS- β gal under both control and arsenite stress conditions, as expected, but noted increased cytoplasmic levels of this protein under both conditions in the presence of ataxin-1[85Q] (Figure 4A, denoted by arrows). This was confirmed by image analysis to determine the nuclear to cytoplasmic ratio (Fn/c) (Figure 4B).

Other nuclear import pathways are selectively influenced by polyQ-ataxin-1

To extend our survey of nuclear transporters in the presence of polyQ-ataxin-1 expression at the single cell level, we next evaluated additional nuclear transport proteins. Comparable to our initial findings (Figure 3), we observed mislocalisation of both importin-13 (IMP13)³⁹ (Fig 5A), and Hikeshi, a non-importin that is responsible for nuclear import of heat shock protein 70 (HSP70) in response to heat shock⁴⁰ (Fig 5B). Both GFP-IMP13 and -Hikeshi were primarily nuclear in the presence or absence of arsenite stress, but showed partial colocalization with ataxin-1[85Q] under control conditions, with colocalization with polyQ-ataxin-1 nuclear bodies in the presence of arsenite-induced stress. Consistent with these observations, we observed alterations in the nucleocytoplasmic distribution for the IMP13 cargo, transcription factor NF-YB⁴¹ (Fig 5C), and the Hikeshi cargo, HSP70⁴⁰ (Fig 5D), both showing partial nuclear colocalization with ataxin-1[85Q] that was enhanced by arsenite stress treatment (Figure 5C, D).

In contrast to the results above, we observed that a number of other nuclear transporters proteins were not impacted by/sequestered into polyQ-ataxin-1 nuclear bodies. Specifically, GFP-IMP α 4, -IMP7, and -IMP16 did not show recruitment into the polyQ-ataxin-1 nuclear bodies under control or arsenite stress conditions (Figure S1A-C). GFP-IPO5 (IMP5), in contrast, appeared to localise to the polyQ-ataxin-1 nuclear structures, but only in the absence of arsenite-induced stress (Figure S1D, denoted by arrowheads in Zoom panel). Taken together, these observations highlight selectivity in the impact of the polyQ-ataxin-1 nuclear bodies by disrupting multiple, but by not all, nuclear import pathways.

The nuclear protein transport pathways mediated by importins/exportins are Ran-dependent and so we next assessed any impact of polyQ-ataxin-1 on RanGTP/GDP distribution through altering localization of its regulators, the Ran GTPase activating protein RanGAP1, and the Ran guanine nucleotide exchanger RCC1. RanGAP1 can localize with mutant huntingtin or C9orf72 polyGA aggregates in *in vivo* models of HD and ALS^{14, 15}, but we observed no alteration in RanGAP1 subcellular distribution in the presence of polyQ-ataxin-1 expression (Figure S2). With our proteomics data identifying RanGAP1, as well as Ran binding protein 1 (RanBP1), in association with GFP-ataxin-1[85Q] in our pulldown analysis (Supplementary Table S1), the implication is that significant mislocalization of RanGAP1 requires longer term exposure to polyQ-ataxin-1 aggregates, as observed for huntingtin-RanGAP1 association in vivo¹⁵. In contrast, our assessment of endogenous RCC1 or ectopically addressed GFP-RCC1

revealed clear colocalisation with polyQ-ataxin-1 nuclear bodies (Figure S3A,B). Thus, through sequestering RCC1 into distinct nuclear bodies, polyQ-ataxin-1 has the potential to reduce nuclear RanGTP levels, and hence importin/exportin-dependent nuclear trafficking. Additionally, not all RCC1 is sequestered into polyQ-ataxin-1 nuclear bodies, explaining how there is not complete disruption of the localization of all nuclear transporters/nuclear transport pathways. Furthermore, that Ran-independent (Hikeshi) and Ran-dependent (importins/exportins) nuclear transport pathways are impacted by polyQ-ataxin-1 expression suggests that there may be additional effects at the level of the nuclear pore complex (NPC).

PolyQ-ataxin-1 expression results in mislocalisation of nucleoporin NUP98

The NPC is the regulated gateway for trafficking between the cell cytosol and nucleus, and is a potential target of mutant polyQ-huntingtin protein in HD¹⁶, where progressive disruption of nuclear envelope morphology has been observed in aging mice expressing the polyQ-huntingtin protein¹⁵. Post-mortem samples from patients with ALS⁴² also show disruptions to the nuclear envelope, whereas polyQ-ataxin-1 may also decrease nuclear membrane instability⁴³.

We set out to evaluate the effect of short-term expression of polyQ-ataxin-1, initially by assessing NPC distribution using the anti-nucleoporin (Nup) Mab414 antibody; no marked changes in staining were observed upon polyQ-ataxin-1 expression (Figure 6A) indicating no wide-spread disruption of NPC distribution in the nuclear envelope. Indicative of general NPC functionality, nuclear accumulation of the transcription factor AF10, known to be importin/Ran-independent and to occur via direct interaction with NPC components^{44, 45} was not affected by polyQ-ataxin-1 (Figure S4). Nucleoporin protein NUP62, within the central core of the NPC^{46, 47}, was not altered in the presence of polyQ-ataxin-1 either in the presence or absence of arsenite stress (Figure S5), in contrast to the impact of mutant huntingtin in HD¹⁶. Importantly, although NUP62 staining showed distinctive nuclear puncta, these did not co-localise with the polyQ-ataxin-1 nuclear bodies (Figure S5), indicating that the effects of polyQ-ataxin-1 and mutant huntingtin are distinct, although both impact nuclear transport machinery.

We next evaluated NUP98, the most conserved FG-dipeptide motif domain nucleoporin and a major contributor to the NPC permeability barrier^{48, 49}. Indeed, the more cohesive nature of NUP98 GLFG repeat domains compared to the FxFG repeats of other nucleoporins⁵⁰ can drive

the formation of highly concentrated gels⁵¹. Immunostaining of endogenous NUP98 revealed its distribution throughout the cell with recruitment into polyQ-ataxin-1 nuclear bodies (Figure 6B, denoted by white arrowheads in Zoom panels). Analogously, ectopically expressed GFP-NUP98, colocalised with polyQ-ataxin-1 nuclear bodies upon arsenite exposure (Figure 7A). To further dissect the mechanisms contributing to this co-localisation, we evaluated the localisation patterns of three truncation derivatives of NUP98: GFP-NUP98 N-terminal (1-225), GFP-NUP98 GLFG domain (221-504) and GFP-NUP98 C-terminal (506-920). We observed overlap but no enrichment in fluorescence colocalised with the polyQ-ataxin-1 nuclear bodies for the N-terminal or C-terminal constructs (Figure 7B). In contrast, we observed small nuclear puncta for GFP-NUP98 GLFG domain (221-504) even in the absence of polyQ-ataxin-1 (Figure 7B, denoted by open arrowheads in Zoom panels); upon arsenite treatment, striking colocalisation in the larger polyQ-ataxin-1 nuclear bodies was also evident (Figure 7B, denoted by white arrowheads in Zoom panels). Thus, sequestration of NUP98 into the polyQ-ataxin-1 nuclear bodies is dependent on the NUP98 GLFG domain.

Previous studies using knockdown of NUP98 to interrogate its functions have shown selective disruption of Tag-NLS-/importin α/β 1-dependent and M9-NLS-/transportin-1 (TNPO1)-dependent nuclear protein import, but not BIB (“ β -importin-binding”)-NLS-dependent transport, that can be mediated by multiple different importin β s^{20, 52}. To test the possible impact of NUP98 sequestration by polyQ-ataxin-1 nuclear bodies on nuclear transport, we examined the subcellular localisation of GFP-M9-NLS and GFP-BIB-NLS. We found that the extent of nuclear accumulation of GFP-M9-NLS, but not of GFP-BIB-NLS was significantly ($p < 0.05$) increased in the presence of polyQ-ataxin-1 expression and arsenite induced stress (Figure S6). These results further support the observations that some, but not all, nuclear transport processes are disrupted by polyQ-ataxin-1.

The ataxin-1 interactome indicates impacts on multiple intracellular processes beyond nuclear transport

Previous genetic screens have highlighted the impact of nuclear transport proteins across a number of neurodegenerative diseases. In exploring suppressors of C9orf72 repeat expansion toxicity in *Drosophila* ALS model, multiple nuclear pore complex proteins, importins/exportins and Ran regulators have been identified^{13, 14, 53}. The earlier screens for genetic suppressors of ataxin-1-induced neuronal degeneration in a *Drosophila* SCA1 model

previously identified the nucleoporin NUP44A as a suppressor of toxicity^{54, 55}. Our study is the first to investigate the impact of short-term polyQ-ataxin-1 expression on cellular nuclear transport processes, our findings indicating that nuclear transport is directly disrupted by short-term polyQ-ataxin-1 expression. Our proteomics analyses, in combination with our surveying of additional nuclear transporters, Ran regulators and nucleoporins, point to the disruption at multiple critical points across the cellular nuclear transport system.

Our results emphasize that approaches to rescue the nuclear transport disruption by mutant ataxin-1 may ultimately provide new ideas on the possible therapeutic interventions to slow neurodegenerative disease progression in SCA1. Furthermore, the ataxin-1 interactome remains a resource for further exploration. For example, we identified replication protein A1 (Rpa1) by pulldown approaches (Table S1); Rpa1 has been previously identified as having the largest effect on lifespan in the *Drosophila* SCA1 model and has been located at the hub position linked to repair systems such as homologous recombination⁵⁶. Others have implicated genes in the protein folding/heat-shock response or ubiquitin-proteolytic pathways as modifiers of toxicity in models of SCA1⁵⁴ and our proteomics studies have identified multiple heat shock proteins as well as proteins involved in ubiquitination, and ubiquitin itself, as part of the ataxin-1 interactome (Table S1). Ataxin-1 phosphorylation may also influence ataxin-1 stability⁵⁷; with the implication of cAMP-dependent protein kinase as a mediator of phosphorylation and toxicity of ataxin-1^{58, 59}, it is of interest that we identified both regulatory and catalytic subunits of cAMP-dependent protein kinase in our interactome analysis (Supplementary Table S1). Increasing levels of wild-type ataxin-1 are sufficient to lead to SCA1-like neurodegeneration⁶⁰, and thus the exact balance of binding partner selection by ataxin-1 is of critical importance. Deciphering the cellular events underlying the ataxin-1 interactome may well be the key to new treatment options for SCA1 and other neurodegenerative diseases.

Materials and methods

Plasmids

The GFP-ataxin-1[85Q] plasmid was provided by D Hatters (University of Melbourne). Myc-BioID (MBI)-ataxin-1[85Q], the myc-tagged BirA* N-terminal fusion with ataxin-1[85Q], was generated by amplifying the coding region of ataxin-1[85Q] from the GFP-ataxin-1[85Q]

construct to include the desired restriction enzyme sites (EcoRI and HindIII), and then ligation into the pcDNA3.1_mycBioID plasmid²⁹ (#35700, addgene). The PCR primer pairs used were 5'-GCGAATTCATGAAATCCAACCAAGAGCGGAGC-3' (forward) and 5'-GCAAGCTTCTACTTGCCTACATTAGACCGGCC-3' (reverse). All constructs were validated by restriction digestion and full sequence analysis.

Cell culture, transfection and treatment

Mouse neuroblastoma cells (Neuro-2a) were cultured in Opti-MEM supplemented with 2 mM L-glutamine (Gibco), 10% fetal bovine serum (BOVOGEN) and 100 U/ml penicillin/streptomycin (Gibco). Cells were plated and cultured (16 h), transfected with the indicated constructs using Lipofectamine 2000 reagent (Invitrogen) according to the manufacturer's instructions (24 h), and then exposed as indicated to 300 μ M sodium arsenite (Sigma) for 1 h. GFP was included as a control for imaging and proteomics protocols examining GFP-ataxin-1[85Q]. When BioID protocols were used, biotin (50 μ M) was included during the transfection protocols with the MBI vector (for blot detection) or MBI-ataxin-1[85Q] (for blot detection or proteomics protocols).

Cell lysate preparation and pull-down protocols

Cell lysates were prepared using RIPA buffer [50 mM Tris-HCl, pH 7.3, 150 mM NaCl, 0.1 mM ethylenediaminetetraacetic acid (EDTA), 1% sodium deoxycholate, 1% Triton X-100, 0.2% NaF and 100 μ M Na₃VO₄] supplemented with complete protease inhibitor mix (Roche Diagnostic). Cell lysates were incubated on ice (20 min) and cleared by centrifugation (1,000 rpm, 20 min). Protein concentrations were determined using the BioRad assay.

For BioID pull-down prior to mass spectrometry or immunoblot analysis, whole cell lysates (3 mg protein) prepared from Neuro-2a cells expressing MBI-ataxin-1[85Q] were incubated with streptavidin-agarose (0.05 mL) (Invitrogen). For GFP pull-down prior to mass spectrometry or immunoblot analysis, whole cell lysates prepared from Neuro-2a cells expressing GFP fusion constructs (3 mg protein) were incubated with GFP-trap-agarose (0.05 mL) (ChromoTek). The incubation for streptavidin-agarose was overnight at 4°C, and for GFP-trap-agarose was 2 h at room temperature. The immobilized proteins in the streptavidin- or GFP-trap-agarose pellets were thoroughly washed. For both protocols, 7 wash steps were performed, with centrifugation (12,000 rpm, 1 min) between washes and with the first 2 washes using RIPA buffer. For the

BioID pull-down, the 5 subsequent wash steps included: 0.5% SDS in PBS (washes 3 and 4), 6 M urea in 100 mM TrisHCl pH 8.5 (washes 5 and 6), and 100 mM TrisHCl pH 8.5 (wash 7). For the GFP pull-down, all 5 subsequent washes used 10 mM Tris-HCl pH 7.5, 150 mM NaCl, 0.5 mM EDTA (washes 3 to 7).

Blot detection of biotinylated proteins

Proteins binding to the streptavidin-agarose were eluted with concentrated SDS-sample buffer (180 mM TrisHCl pH 6.8, 30% glycerol, 6% SDS, 0.06% bromophenol blue, 15% β -mercaptoethanol). Samples were boiled (5 min, 95°C). Eluted proteins were separated by SDS-PAGE (8% polyacrylamide gels, 1.5 h) and transferred to polyvinylidene difluoride (PVDF) membranes (Amersham Life Science; 2 h, room temperature). Subsequent steps were performed by blocking with 1% bovine serum albumin (BSA) in phosphate-buffered saline (PBS; 0.5 h, room temperature), and incubating with streptavidin-HRP (Invitrogen, 1:2000; 1h, room temperature) followed by thorough washing with Tris-buffered saline Tween-20 (TBST). The membrane was finally blocked with buffer (1% BSA, 1% Triton X-100 in PBS; 5 min), washed (TBST, 3 x 1 min), and visualised using an enhanced chemiluminescence detection system (ThermoFisher Scientific). Images were captured using ChemiDoc imager (Bio-Rad) operating in a single-channel protocol.

Mass spectrometry (MS) analysis

Proteins in the washed streptavidin- or GFP-trap-agarose pellets were further prepared for MS analysis. For streptavidin-agarose pellets, an on-bead digestion was performed by adding 20 μ l trypsin-containing denaturing solution (50 mM urea, 5 mM tris(2-carboxyethyl) phosphine (TCEP) and 0.25 μ g trypsin (Sigma) in 50 mM triethylammonium bicarbonate (TEAB)). After incubation (overnight, 37°C, end-over-end rotation), supernatants were collected. For the GFP-trap-agarose pellets, an in-solution digestion for the eluted proteins was performed by adding the elution solution (50% aqueous 2,2,2-Trifluoroethanol (TFE)/0.05% formic acid, pH 2.0, 1mM TCEP). After incubation (5 min, room temperature), supernatants were collected and then 40 μ L trypsin solution (0.25 μ g trypsin, 200 mM TEAB) added before incubation (overnight, 37°C, end-over-end rotation).

For each trypsin-digested sample, supernatant (10 μ l) was collected and tryptic peptides were analysed by liquid chromatography-MS/MS (LC-MS/MS) using an Q-Exactive plus mass

spectrometer (Thermo Scientific) fitted with nanoflow reversed-phase-HPLC (Ultimate 3000 RSLC, Dionex). The nano-LC system was equipped with an Acclaim Pepmap nano-trap column (Dionex – C18, 100 Å, 75 µm × 2 cm) and an Acclaim Pepmap RSLC analytical column (Dionex – C18, 100 Å, 75 µm × 50 cm). Typically for each LC-MS/MS experiment, 1 µL supernatant was loaded onto the enrichment (trap) column (isocratic flow 5 µL/min, 3% CH₃CN containing 0.1% formic acid, 6 min) before the enrichment column was switched in-line with the analytical column. For LC, the eluents used were 0.1% formic acid (solvent A) and 100% CH₃CN/0.1% formic acid (solvent B) with the following sequence of gradients: 3 to 20% B (in 95 min), 20 to 40% B (in 10 min), 40 to 80% B (in 5 min), 80% B (maintained for the final 5 min) before equilibration in 3% B prior to the next analysis (10 min). All spectra were acquired in positive mode with full scan MS1 scanning from m/z 375-1400 (70000 resolution, AGC target 3e6, maximum accumulation time 50 ms, lockmass 445.120024). The 15 most intense peptide ions with charge states ≥2-5 were isolated (isolation window 1.2 m/z) and fragmented with normalized collision energy of 30 (35000 resolution, AGC target 1e5, maximum accumulation time 50 ms). An underfill threshold was set to 2% for triggering of precursor for MS2. Dynamic exclusion was activated for 30s.

Bioinformatic analysis

Resultant MS/MS data was analyzed using the Mascot search engine (Matrix Science version 2.4) against the SWISSPROT database (with the settings as follows: taxonomy - Mus., enzyme - Trypsin, Protein Mass - ± 20 ppm, Fragment Mass Tolerance - ± 0.2 Da, Max Missed Cleavages: 2). Identifications in all samples (test or background/non-specific binding) were accepted for proteins with at least two significant peptides (p<0.05). Background/non-specific binding proteins were identified as follows: for the Pulldown protocol assessments, proteins identified in samples prepared from GFP only-transfected cells processed in parallel in each of the 3 replicates were defined as background/non-specific binding; for BioID assessments, proteins identified in samples prepared from untransfected cells across all 3 replicates were pooled and defined as background as endogenously biotinylated proteins. Proteins in the resulting lists were retained for further consideration when they were identified in at least three of the four tested conditions (BioID ± arsenite; Pulldown ± arsenite) were further considered. Ingenuity pathway analysis (IPA; QIAGEN) was carried out according to the supplier's instructions with default settings.

Immunofluorescence, confocal laser scanning microscopy and image analysis

Neuro-2a cells were cultured on coverslips (Proscitech), transfected and treated with 300 μ M arsenite, as indicated. Subsequent processing (washing, permeabilization (0.2% (v/v) Triton X-100), fixation (4% (w/v) paraformaldehyde and blocking (1% (w/v) bovine serum albumin (BSA)) was performed at room temperature in phosphate-buffered saline. Cells were then incubated sequentially with primary antibodies then fluorophore-conjugated secondary antibodies or streptavidin as indicated, each in 1% (w/v) BSA in PBS for 1 h at room temperature. The primary antibodies used were as follows: anti-cMyc (sc-40, Santa Cruz); anti-NUP, Mab414 (ab24609, abcam); anti-NUP98 (sc-14153, Santa Cruz); anti-NUP62 (610498, BD Biosciences); anti-RanGAP1 (ab2081, ancaml); anti-RCC1 (sc-1162, Santa Cruz). Subsequent detection used Alexa Fluor® 568-conjugated secondary antibodies (A-11004, Invitrogen) or Alexa Fluor® 488-conjugated Streptavidin (S11223, Invitrogen). Processed coverslips were then mounted by water-based Fluoro-Gel (Proscitech) onto glass slides for visualization by confocal laser scanning microscopy (Leica TCS SP5 with 63X 1.4 Oil Objective). Images were analyzed using Fiji software, with quantitative analysis of the fluorescence intensity of nucleus/cytoplasm ratio (Fn/c) performed using CellProfiler cell image analysis software (version 2.1.1 for Mac).

Statistical analysis

Graphpad Prism 6 (version 6.00 for Mac) was used for statistical analysis. For analysis of >2 datasets, ANOVA was applied to compare differences among different datasets, followed by Tukey's multiple comparisons test. Data are represented as mean \pm standard error of the mean (SEM), with $p < 0.05$ regarded as statistically significant.

Author contributions

S.Z., D.A.J. and M.A.B conceived the work and designed the experiments. S.Z. and N.A.W. performed the experiments and all authors analyzed the data. S.Z. drafted the manuscript, and all authors contributed to discussions and reviewed the manuscript.

References

1. Rub U, *et al.* Clinical features, neurogenetics and neuropathology of the polyglutamine spinocerebellar ataxias type 1, 2, 3, 6 and 7. *Progress in neurobiology* **104**, 38-66 (2013).
2. Orr HT, *et al.* Expansion of an unstable trinucleotide CAG repeat in spinocerebellar ataxia type 1. *Nature genetics* **4**, 221-226 (1993).
3. Cummings CJ, Orr HT, Zoghbi HY. Progress in pathogenesis studies of spinocerebellar ataxia type 1. *Philosophical transactions of the Royal Society of London Series B, Biological sciences* **354**, 1079-1081 (1999).
4. Adegbuyiro A, Sedighi F, Pilkington AWt, Groover S, Legleiter J. Proteins Containing Expanded Polyglutamine Tracts and Neurodegenerative Disease. *Biochemistry* **56**, 1199-1217 (2017).
5. Lasagna-Reeves CA, *et al.* A native interactor scaffolds and stabilizes toxic ATAXIN-1 oligomers in SCA1. *Elife* **4**, (2015).
6. Chen M, Wolynes PG. Aggregation landscapes of Huntingtin exon 1 protein fragments and the critical repeat length for the onset of Huntington's disease. *Proceedings of the National Academy of Sciences of the United States of America* **114**, 4406-4411 (2017).
7. Wen J, Scoles DR, Facelli JC. Molecular dynamics analysis of the aggregation propensity of polyglutamine segments. *PloS one* **12**, e0178333 (2017).
8. Ingram M, *et al.* Cerebellar Transcriptome Profiles of ATXN1 Transgenic Mice Reveal SCA1 Disease Progression and Protection Pathways. *Neuron* **89**, 1194-1207 (2016).
9. Ashkenazi A, *et al.* Polyglutamine tracts regulate autophagy. *Autophagy*, 1-2 (2017).
10. Nath SR, Lieberman AP. The Ubiquitination, Disaggregation and Proteasomal Degradation Machineries in Polyglutamine Disease. *Front Mol Neurosci* **10**, 78 (2017).
11. Ramdzan YM, *et al.* Huntingtin Inclusions Trigger Cellular Quiescence, Deactivate Apoptosis, and Lead to Delayed Necrosis. *Cell reports* **19**, 919-927 (2017).
12. Sambataro F, Pennuto M. Post-translational Modifications and Protein Quality Control in Motor Neuron and Polyglutamine Diseases. *Front Mol Neurosci* **10**, 82 (2017).
13. Freibaum BD, *et al.* GGGGCC repeat expansion in C9orf72 compromises nucleocytoplasmic transport. *Nature* **525**, 129-133 (2015).
14. Zhang K, *et al.* The C9orf72 repeat expansion disrupts nucleocytoplasmic transport. *Nature* **525**, 56-61 (2015).
15. Gasset-Rosa F, *et al.* Polyglutamine-Expanded Huntingtin Exacerbates Age-Related Disruption of Nuclear Integrity and Nucleocytoplasmic Transport. *Neuron* **94**, 48-57 e44 (2017).

16. Grima JC, *et al.* Mutant Huntingtin Disrupts the Nuclear Pore Complex. *Neuron* **94**, 93-107 e106 (2017).
17. Cautain B, Hill R, de Pedro N, Link W. Components and regulation of nuclear transport processes. *FEBS J* **282**, 445-462 (2015).
18. Freitas N, Cunha C. Mechanisms and signals for the nuclear import of proteins. *Curr Genomics* **10**, 550-557 (2009).
19. Sorokin AV, Kim ER, Ovchinnikov LP. Nucleocytoplasmic transport of proteins. *Biochemistry (Mosc)* **72**, 1439-1457 (2007).
20. Wu X, Kasper LH, Mantcheva RT, Mantchev GT, Springett MJ, van Deursen JM. Disruption of the FG nucleoporin NUP98 causes selective changes in nuclear pore complex stoichiometry and function. *Proceedings of the National Academy of Sciences of the United States of America* **98**, 3191-3196 (2001).
21. Azuma Y, Dasso M. The role of Ran in nuclear function. *Curr Opin Cell Biol* **12**, 302-307 (2000).
22. Okazawa H, *et al.* Interaction between mutant ataxin-1 and PQBP-1 affects transcription and cell death. *Neuron* **34**, 701-713 (2002).
23. Dovey CL, Varadaraj A, Wyllie AH, Rich T. Stress responses of PML nuclear domains are ablated by ataxin-1 and other nucleoprotein inclusions. *The Journal of pathology* **203**, 877-883 (2004).
24. Bolger TA, Zhao X, Cohen TJ, Tsai CC, Yao TP. The neurodegenerative disease protein ataxin-1 antagonizes the neuronal survival function of myocyte enhancer factor-2. *Journal of Biological Chemistry* **282**, 29186-29192 (2007).
25. Prakash C, Soni M, Kumar V. Biochemical and Molecular Alterations Following Arsenic-Induced Oxidative Stress and Mitochondrial Dysfunction in Rat Brain. *Biol Trace Elem Res* **167**, 121-129 (2015).
26. Yu CW, Liao VH. Arsenite induces neurotoxic effects on AFD neurons via oxidative stress in *Caenorhabditis elegans*. *Metallomics* **6**, 1824-1831 (2014).
27. Matilla A, Koshy BT, Cummings CJ, Isobe T, Orr HT, Zoghbi HY. The cerebellar leucine-rich acidic nuclear protein interacts with ataxin-1. *Nature* **389**, 974-978 (1997).
28. Al-Ramahi I, *et al.* CHIP protects from the neurotoxicity of expanded and wild-type ataxin-1 and promotes their ubiquitination and degradation. *The Journal of biological chemistry* **281**, 26714-26724 (2006).
29. Roux KJ, Kim DI, Raida M, Burke B. A promiscuous biotin ligase fusion protein identifies proximal and interacting proteins in mammalian cells. *The Journal of cell biology* **196**, 801-810 (2012).

30. Lambert JP, Tucholska M, Go C, Knight JD, Gingras AC. Proximity biotinylation and affinity purification are complementary approaches for the interactome mapping of chromatin-associated protein complexes. *Journal of proteomics* **118**, 81-94 (2015).
31. Hosp F, *et al.* Quantitative interaction proteomics of neurodegenerative disease proteins. *Cell reports* **11**, 1134-1146 (2015).
32. Lam YC, *et al.* ATAXIN-1 interacts with the repressor Capicua in its native complex to cause SCA1 neuropathology. *Cell* **127**, 1335-1347 (2006).
33. de Chiara C, Pastore A. Kaleidoscopic protein-protein interactions in the life and death of ataxin-1: new strategies against protein aggregation. *Trends in neurosciences* **37**, 211-218 (2014).
34. Lu HC, *et al.* Disruption of the ATXN1-CIC complex causes a spectrum of neurobehavioral phenotypes in mice and humans. *Nature genetics* **49**, 527-536 (2017).
35. Stade K, Ford CS, Guthrie C, Weis K. Exportin 1 (Crm1p) is an essential nuclear export factor. *Cell* **90**, 1041-1050 (1997).
36. Miyamoto Y, *et al.* Importin alpha can migrate into the nucleus in an importin beta- and Ran-independent manner. *Embo Journal* **21**, 5833-5842 (2002).
37. Shao X, Kawauchi K, Shivashankar GV, Bershadsky AD. Novel localization of formin mDia2: importin beta-mediated delivery to and retention at the cytoplasmic side of the nuclear envelope. *Biol Open* **4**, 1569-1575 (2015).
38. Wu Z, Jiang Q, Clarke PR, Zhang C. Phosphorylation of Crm1 by CDK1-cyclin-B promotes Ran-dependent mitotic spindle assembly. *Journal of cell science* **126**, 3417-3428 (2013).
39. Mingot JM, Kostka S, Kraft R, Hartmann E, Gorlich D. Importin 13: a novel mediator of nuclear import and export. *Embo Journal* **20**, 3685-3694 (2001).
40. Kose S, Furuta M, Imamoto N. Hikeshi, a Nuclear Import Carrier for Hsp70s, Protects Cells from Heat Shock-Induced Nuclear Damage. *Cell* **149**, 578-589 (2012).
41. Kahle J, Baake M, Doenecke D, Albig W. Subunits of the heterotrimeric transcription factor NF-Y are imported into the nucleus by distinct pathways involving importin beta and importin 13. *Molecular and Cellular Biology* **25**, 5339-5354 (2005).
42. Kinoshita Y, *et al.* Nuclear contour irregularity and abnormal transporter protein distribution in anterior horn cells in amyotrophic lateral sclerosis. *J Neuropathol Exp Neurol* **68**, 1184-1192 (2009).
43. Mapelli L, *et al.* Toxic effects of expanded ataxin-1 involve mechanical instability of the nuclear membrane. *Biochimica et biophysica acta* **1822**, 906-917 (2012).
44. Cai Y, *et al.* Characterization and potential function of a novel testis-specific nucleoporin BS-63. *Mol Reprod Dev* **61**, 126-134 (2002).

45. Lieu KG, *et al.* The p53-induced factor Ei24 inhibits nuclear import through an importin beta-binding-like domain. *The Journal of cell biology* **205**, 301-312 (2014).
46. Knockenhauer KE, Schwartz TU. The Nuclear Pore Complex as a Flexible and Dynamic Gate. *Cell* **164**, 1162-1171 (2016).
47. Griffis ER, Altan N, Lippincott-Schwartz J, Powers MA. Nup98 is a mobile nucleoporin with transcription-dependent dynamics. *Mol Biol Cell* **13**, 1282-1297 (2002).
48. Hulsman BB, Labokha AA, Gorlich D. The permeability of reconstituted nuclear pores provides direct evidence for the selective phase model. *Cell* **150**, 738-751 (2012).
49. Schmidt HB, Gorlich D. Transport Selectivity of Nuclear Pores, Phase Separation, and Membraneless Organelles. *Trends in biochemical sciences* **41**, 46-61 (2016).
50. Xu S, Powers MA. In vivo analysis of human nucleoporin repeat domain interactions. *Mol Biol Cell* **24**, 1222-1231 (2013).
51. Labokha AA, *et al.* Systematic analysis of barrier-forming FG hydrogels from *Xenopus* nuclear pore complexes. *The EMBO journal* **32**, 204-218 (2013).
52. Jakel S, Gorlich D. Importin beta, transportin, RanBP5 and RanBP7 mediate nuclear import of ribosomal proteins in mammalian cells. *The EMBO journal* **17**, 4491-4502 (1998).
53. Boeynaems S, *et al.* Drosophila screen connects nuclear transport genes to DPR pathology in c9ALS/FTD. *Scientific reports* **6**, 20877 (2016).
54. Fernandez-Funez P, *et al.* Identification of genes that modify ataxin-1-induced neurodegeneration. *Nature* **408**, 101-106 (2000).
55. Branco J, *et al.* Comparative analysis of genetic modifiers in *Drosophila* points to common and distinct mechanisms of pathogenesis among polyglutamine diseases. *Human molecular genetics* **17**, 376-390 (2008).
56. Barclay SS, *et al.* Systems biology analysis of *Drosophila* in vivo screen data elucidates core networks for DNA damage repair in SCA1. *Human molecular genetics* **23**, 1345-1364 (2014).
57. Jorgensen ND, Andresen JM, Pitt JE, Swenson MA, Zoghbi HY, Orr HT. Hsp70/Hsc70 regulates the effect phosphorylation has on stabilizing ataxin-1. *Journal of neurochemistry* **102**, 2040-2048 (2007).
58. Jorgensen ND, *et al.* Phosphorylation of ATXN1 at Ser776 in the cerebellum. *Journal of neurochemistry* **110**, 675-686 (2009).
59. Hearst SM, Shao Q, Lopez M, Raucher D, Vig PJ. The design and delivery of a PKA inhibitory polypeptide to treat SCA1. *Journal of neurochemistry* **131**, 101-114 (2014).

60. Gennarino VA, *et al.* Pumilio1 Haploinsufficiency Leads to SCA1-like Neurodegeneration by Increasing Wild-Type Ataxin1 Levels. *Cell* **160**, 1087-1098 (2015).

FIGURES

Figure 1. Ataxin-1[85Q] forms distinctive nuclear bodies enhanced by arsenite-induced stress.

Neuro-2a cells were transfected to express either GFP-vector or GFP-ataxin-1[85Q] (A) or MBI-vector or MBI-ataxin-1[85Q] with simultaneous addition of biotin (50 μ M) (B-D). At 24 h post-transfection, cells were treated with arsenite (300 μ M, 1 h) as indicated. Cells were then fixed and stained with DAPI (A), or fixed, stained with anti-myc antibody, Alexa 488-streptavidin and DAPI (C), before confocal laser scanning microscopy (CLSM) imaging. Representative images are shown from 3 independent experiments; merge panels overlay GFP and DAPI images (A) or anti-myc, streptavidin and DAPI images (C), respectively. Scale bars = 10 μ m. (B) Workflow for BioID sample validation and ataxin-1[85Q] interactome analysis in Neuro-2a cells. (D) At 24 h post-transfection, cells were lysed and lysates subjected to SDS-PAGE, with biotinylated proteins subsequently detected using streptavidin-HRP. Results are typical of 2 independent experiments.

Figure 2. Combined approaches to ataxin-1[85Q] interactome identification reveal enrichment of nuclear transport proteins.

(A, B) Parallel workflows for sample preparation for mass spectrometry to identify the ataxin-1[85Q] interactome in Neuro-2a cells (\pm arsenite treatment, 300 μ M, 1 h). (A) The BioID protocol included the control without transfection or the expression of MBI-ataxin-1[85Q] with the simultaneous addition of biotin (50 μ M) for 24 h, whereas the Pulldown protocol included the expression of GFP or GFP-ataxin-1[85Q] for 24 h. Following cell lysis, proteins were captured then subjected to trypsin digestion as indicated. (B) Mass spectrometry MASCOT analysis identified peptides from the 4 treatment conditions (BioID \pm arsenite; Pulldown \pm arsenite) that were matched to the protein reference library SWISSPROT (Mus musculus). Refinement of identified proteins included discarding those proteins identified by < 2 peptides and those that appeared in background control samples (i.e. for no transfection or GFP alone). Of 675 proteins identified, 91 proteins were consistently shared by ≥ 3 conditions across biological triplicate samples. (C) Venn diagram overview of the 675 identified proteins, grouped according to cell exposure (\pm arsenite treatment) and sample preparation (BioID or Pulldown). Areas marked by asterisk indicate those groupings of proteins identified in ≥ 3 conditions. (D) Ingenuity Pathway Analysis (IPA) was performed on the 91 proteins

consistently shared by ≥ 3 conditions across biological triplicate samples. The top-ranked category as assessed by the $-\log(\text{p-value})$, RAN Signaling, represents nuclear transport proteins.

Figure 3. The classical nuclear import proteins, importin- α 2 and importin- β 1, as well as the exporter exportin-1, partially co-localise with the ataxin-1[85Q] nuclear structures.

Neuro-2a cells were cotransfected to express MBI-ataxin-1[85Q] together with (A) GFP-Importin- α 2 (IMP α 2), (B) GFP-Importin- β 1 (IMP β 1), (C) GFP-CRM1, or (D) GFP alone. At 24 h post-transfection, cells were treated with arsenite as indicated, and then fixed, stained with anti-myc antibodies and DAPI, before CLSM imaging. Representative images of cells from 2 independent experiments are shown, with zoom images (right panels) corresponding to the boxed regions. Increased co-localization, by accumulation in the ataxin-1 nuclear bodies, is indicated by the white arrowheads. Scale bar = 10 μm .

Figure 4. Reduced nuclear accumulation of the conventional importin- α / β 1-recognised cargo GFP-TagNLS- β -galactosidase in the presence of ataxin-1[85Q].

Neuro-2a cells were cotransfected to express MBI-ataxin-1[85Q] together with GFP-TagNLS- β -galactosidase (GFP-NLS- β Gal). At 24 h post-transfection, cells were treated with arsenite as indicated, and then fixed, stained with anti-myc antibody and DAPI, before CLSM imaging. (A) Representative images from 2 independent experiments are shown; merge panels overlay GFP, myc, and DAPI images. Zoom images (right panels) correspond to the boxed regions and the position of the nucleus as determined by DAPI staining is indicated by the white dashed lines. Thin white arrows denote increased cytoplasmic fluorescence in the presence of MBI-ataxin-1[85Q]. Scale bar = 10 μm . (B) Integrated fluorescence intensity in nucleus (n) and cytoplasm (c) was estimated and the nuclear to cytoplasmic fluorescence ratio (Fn/c) determined using a modified CellProfiler pipeline. Results represent the mean \pm SEM (n > 25). *** p<0.001, n.s. not significant).

Figure 5. Ataxin-1[85Q] alters Importin-13 and Hikeshi localization, impacting their transport activity.

Neuro-2a cells were transfected to coexpress MBI-ataxin-1[85Q] with (A) GFP-Importin-13 (GFP-IMP13), (B) GFP-Hikeshi, (C) IMP13 cargo protein NF-YB-GFP or (D) Hikeshi cargo protein GFP-HSP70. At 24 h post-transfection, cells were treated with arsenite as indicated,

and then fixed, stained with anti-myc antibody and DAPI, before CLSM imaging. Representative images from 2 independent experiments are shown; merge panels overlay GFP, myc, and DAPI images. Zoom images (right panels) correspond to the boxed regions; colocalization in MBI-ataxin-1[85Q] nuclear bodies is denoted by the white arrowheads. Scale bar = 10 μ m.

Figure 6. Ataxin-1[85Q] expression alters NUP98 localization but not general NPC distribution.

Neuro-2a cells were transfected to express MBI-ataxin-1[85Q] and treated with arsenite as indicated at 24 h post-transfection. Cells were then fixed, stained with anti-NPC (Mab414) (A) or anti-NUP98 (B) antibodies together with DAPI, before CLSM imaging. Representative images from 2 independent experiments are shown; merge panels overlay (A) NPC, GFP, and DAPI or (B) NUP98, GFP, and DAPI images. Zoom images (right panels) correspond to the boxed regions; white arrowheads denote colocalisation in ataxin-1[85Q] nuclear bodies. Scale bar = 10 μ m.

Figure 7. The nucleoporin NUP98 is recruited into ataxin-1[85Q] structures, and this recruitment depends on the NUP98 GLFG repeats.

Neuro-2a cells were transfected to coexpress MBI-ataxin-1[85Q] with GFP-NUP98 (A), or the indicated GFP-NUP98 truncation constructs (B). At 24 h post-transfection., cells were treated with arsenite as indicated, and then fixed, stained with anti-myc-antibodies and DAPI, before CLSM imaging. Representative images from 2 independent experiments are shown; merge panels overlay GFP, myc, and DAPI images. Zoom images (right panels) correspond to the boxed regions. White arrowheads denote colocalization in ataxin-1[85Q] nuclear bodies; NUP98 nuclear puncta are indicated by the open arrowheads. Scale bar = 10 μ m.

Supplementary Figures

Figure S1. Mislocalisation of IPO5 but not IMP α 4, IMP7, IMP16 upon polyQ-ataxin-1 expression.

Neuro-2a cells were cotransfected to express MBI-ataxin-1[85Q] together with (A) GFP-IMP α 4, (B) GFP-Importin-7 (IMP7), (C) GFP-Importin-16 (IMP16) or GFP-Importin-5 (IPO5). At 24 h post-transfection, cells were treated with arsenite as indicated, and then fixed, stained with anti-myc antibody and DAPI, before CLSM imaging. Representative images are shown from 2 independent experiments; zoom images (right panels) correspond to the boxed regions. Scale bar = 10 μ m.

Figure S2. RanGAP1 localisation is unaltered upon polyQ-ataxin-1 expression.

Neuro-2a cells were transfected to express GFP-ataxin-1[85Q]. At 24 h post-transfection, cells were treated with arsenite as indicated, and then fixed, stained with anti-RanGAP1 antibody and DAPI, before CLSM imaging. Representative images are shown from 2 independent experiments; merge panels overlay RanGAP1, GFP, and DAPI images. Zoom images (right panels) correspond to the boxed region. Scale bar = 10 μ m.

Figure S3. RCC1 localizes in poly-ataxin-1 nuclear bodies.

Neuro-2a cells were (A) transfected to express GFP-ataxin-1[85Q] or (B) MB-ataxin-1[85Q] together with GFP-RCC1. At 24 h post-transfection, cells were treated with arsenite as indicated, and then fixed, stained with (A) anti-RCC1 or anti-myc (B) antibodies, and DAPI, before CLSM imaging. Representative images are shown from 2 independent experiments; merge panels overlay (A) RCC1, GFP, and DAPI images (B) GFP, myc, and DAPI images. Zoom images (right panels) correspond to the boxed region; colocalization in MB-ataxin-1[85Q] nuclear bodies is denoted by the white arrowheads. Scale bar = 10 μ m.

Figure S4. Nuclear import of GFP-AF10 is not influenced by polyQ-ataxin-1.

Neuro-2a cells were transfected to coexpress MBI-ataxin-1[85Q] and GFP-AF10. At 24 h post-transfection, cells were treated with arsenite as indicated, and then fixed, stained with anti-myc-antibody and DAPI, before CLSM imaging. Representative images from 2 independent experiments are shown; merge panels overlay GFP, myc and DAPI images. Zoom images (right panels) correspond to the boxed regions. Scale bar = 10 μ m. The position of the nucleus

as determined by DAPI staining is indicated by the white dashed lines. The nuclear to cytoplasmic fluorescence ratio (Fn/c) was calculated by a modified CellProfiler pipeline as per the legend to Figure 4B. Results represent the mean \pm SEM (n > 25); n.s. not significant.

Figure S5. NUP62 localization is not altered by polyQ-ataxin-1 expression.

Neuro-2a cells were transfected to express GFP-ataxin-1[85Q]. At 24 h post-transfection, cells were treated with arsenite as indicated, and then fixed, stained with anti-NUP62 and DAPI, before CLSM imaging. Representative images from 2 independent experiments are shown; merge panels overlay NUP62, GFP, and DAPI images. Zoom images (right panels) correspond to the boxed region. Scale bar = 10 μ m.

Figure S6. M9 NLS nuclear trafficking, but not BIB NLS nuclear trafficking, is disrupted in the presence of polyQ-ataxin-1.

Neuro-2a cells were transfected to coexpress MBI-ataxin-1[85Q] with GFP-M9 NLS (A,B) or GFP-BIB (C,D). At 24 h post-transfection, cells were treated with arsenite as indicated, and then fixed, stained with anti-myc-antibody and DAPI, before CLSM imaging. (A & C) Representative images are shown from 3 independent experiments and merge panels overlay GFP, myc, and DAPI images; the position of the nucleus as determined by DAPI staining is indicated by the white dashed lines. Scale bar = 10 μ m. (B & D) The nuclear to cytoplasmic fluorescence ratio (Fn/c) was calculated by a modified CellProfiler pipeline as per the legend to Figure 4B. Results represent the mean \pm SEM (n > 25); * p<0.05, n.s. not significant.

Supplementary Table S1: Alphabetical listing of the ataxin-1[85Q] interactome identified in Neuro2A cells by BioID and GFP-pulldown approaches

(see separate Excel spreadsheet: Zhang_etal_SUPPTable1.xlsx)

Supplementary Table S2: Nuclear transporters (IPA: RAN Signaling) identified as members of the ataxin-1[85Q] interactome.

Uniprot ID_MOUSE	Encoded protein ^a	Nuclear Transport Role
IMA1	Importin- α 2	Nuclear import receptor (α -family) binding classical NLS-containing proteins; heterodimerises with importin β 1 to facilitate transit through the nuclear pore
IPO5	Importin-5/ Importin- β 3	Nuclear import receptor (β -family) for proteins including some ribosomal proteins and histones
TNPO1	Transportin-1/Importin- β 2	Nuclear import/export receptor (β -family) for proteins including hnRNPs, ribosomal proteins and histones
XPO1	Exportin-1/CRM1	Nuclear export receptor for diverse protein cargoes containing classical leucine-rich NES motifs
XPO2	Exportin-2/CAS	Nuclear export receptor for importin- α

^a Includes alternative names

Figure 1

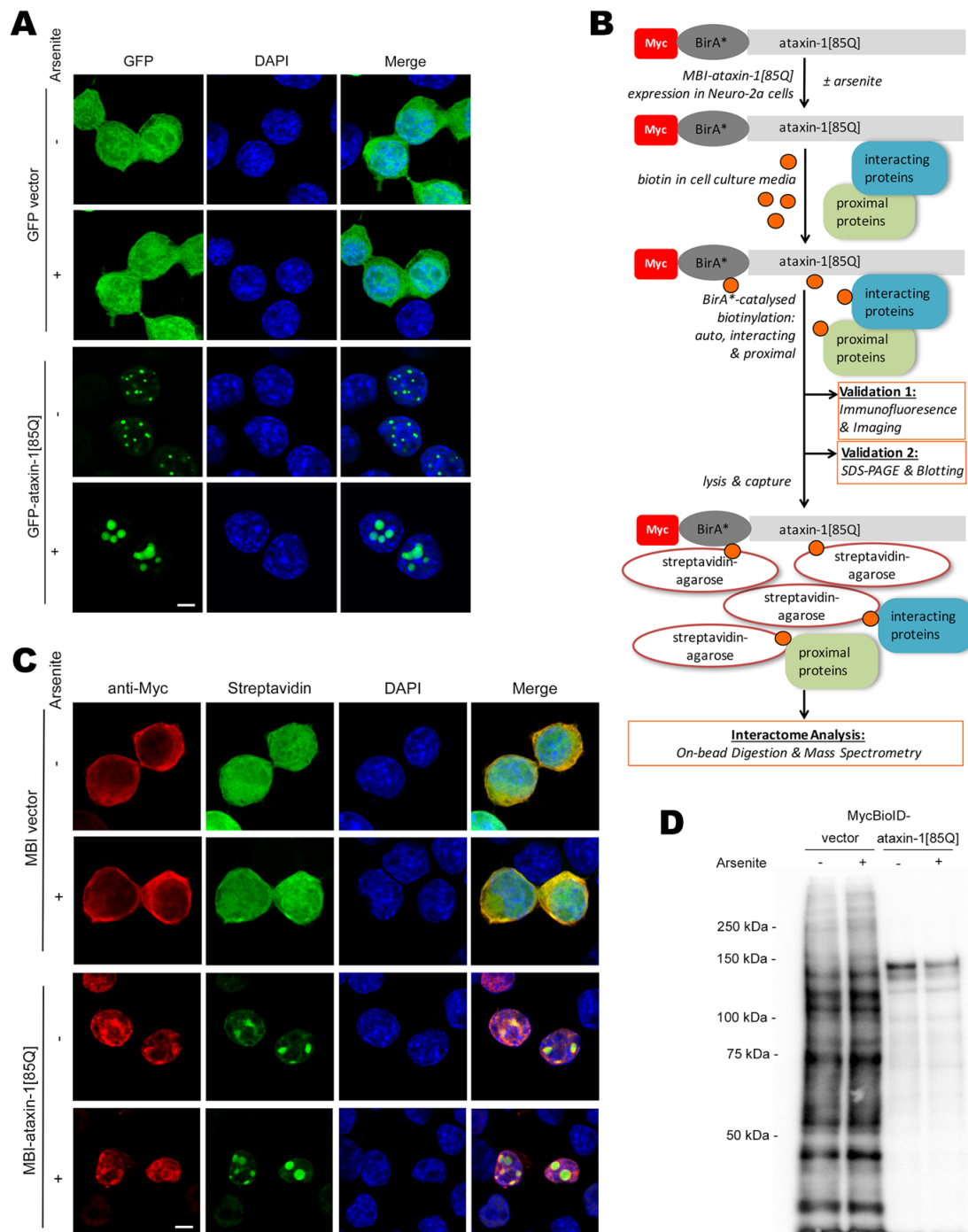


Figure 2

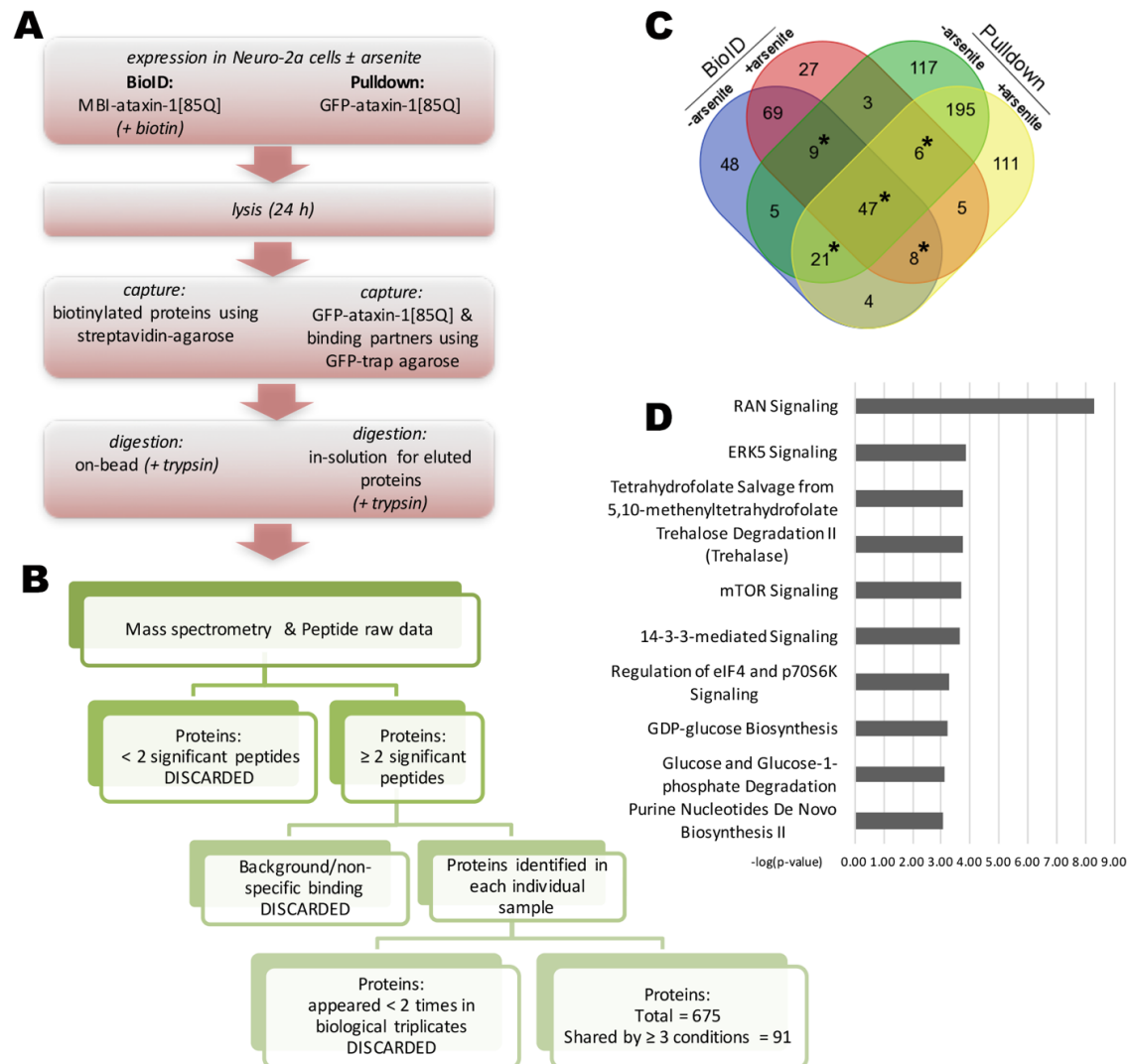


Figure 3

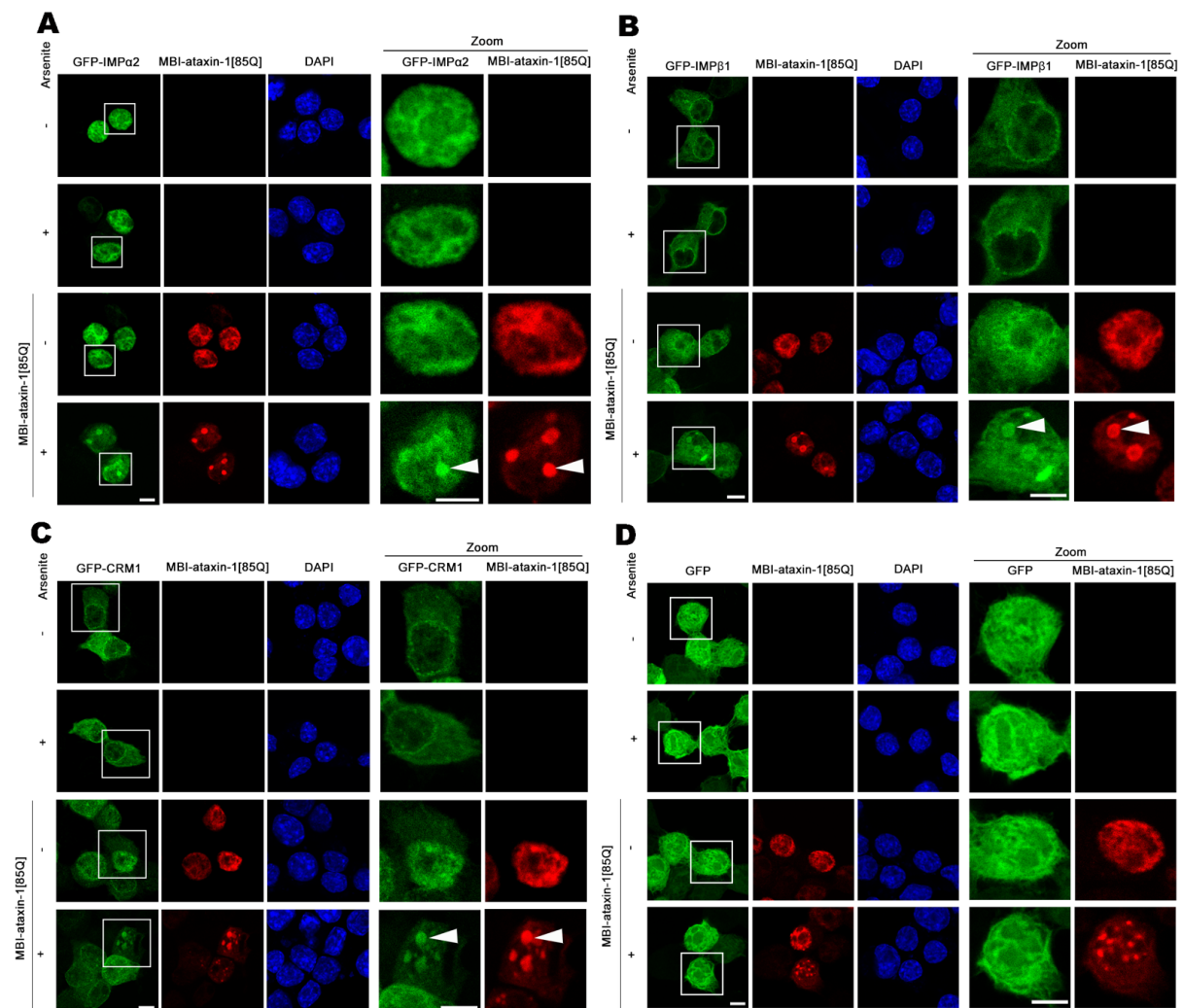


Figure 4

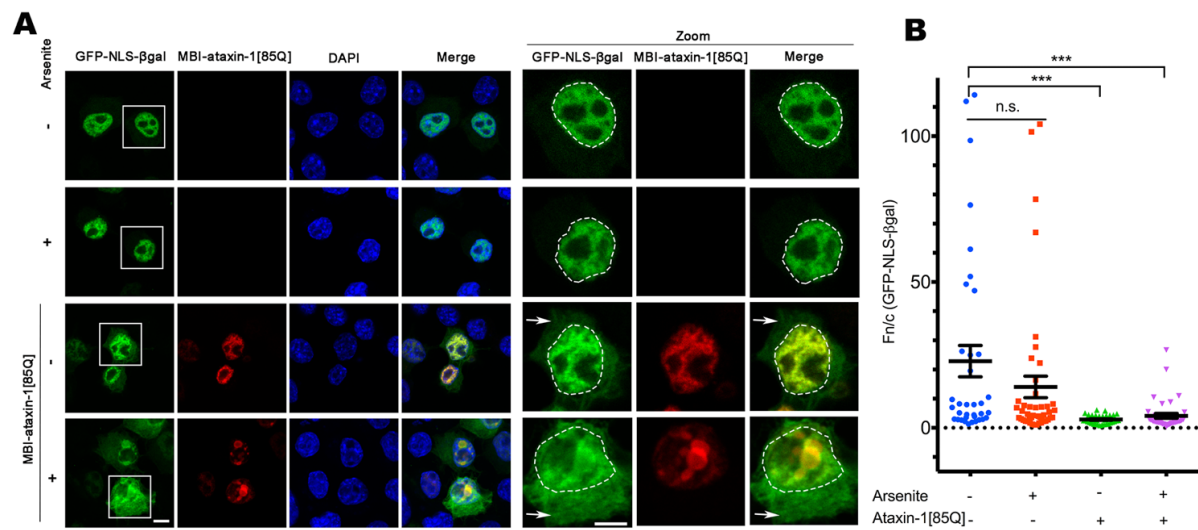


Figure 5

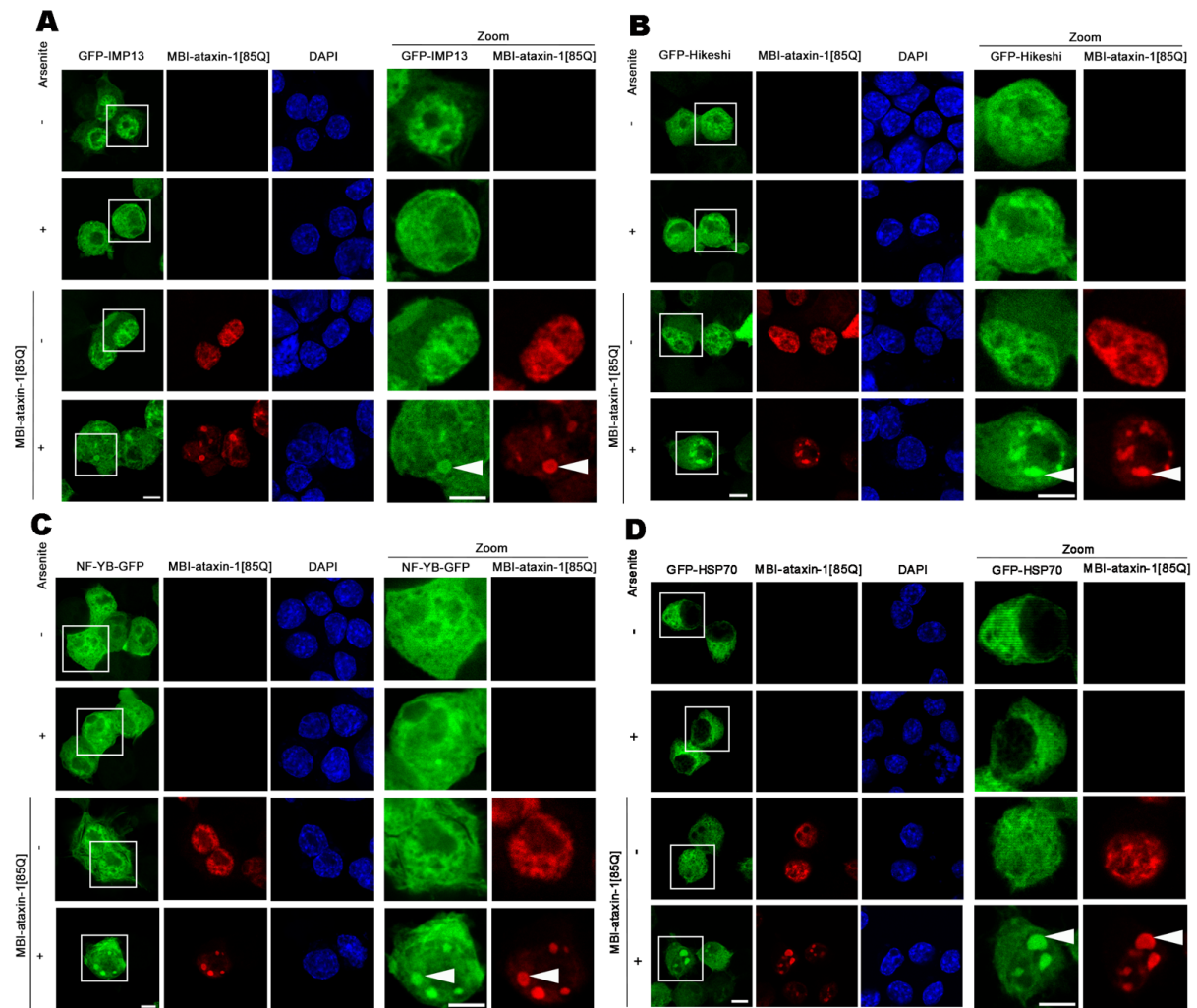


Figure 6

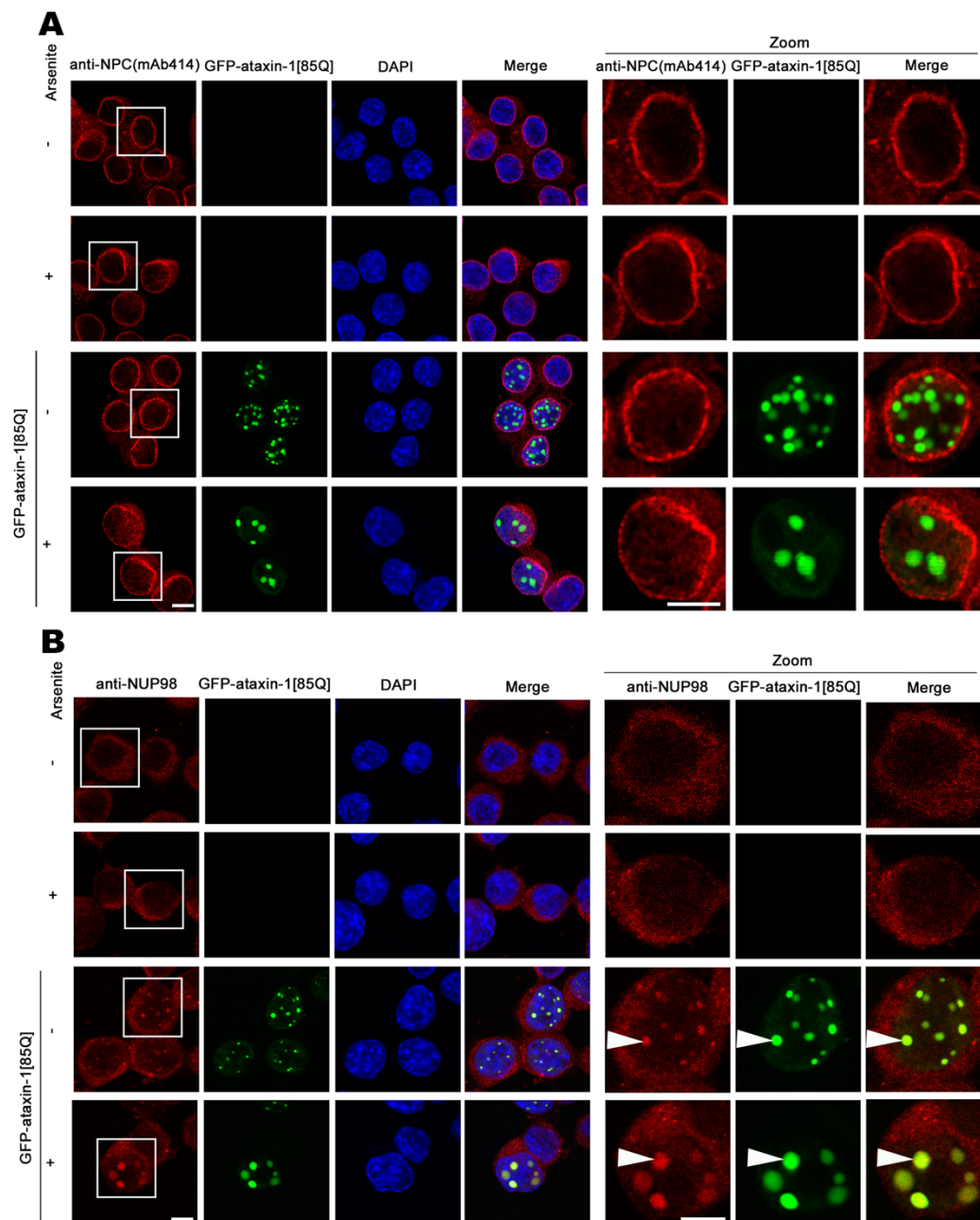


Figure 7

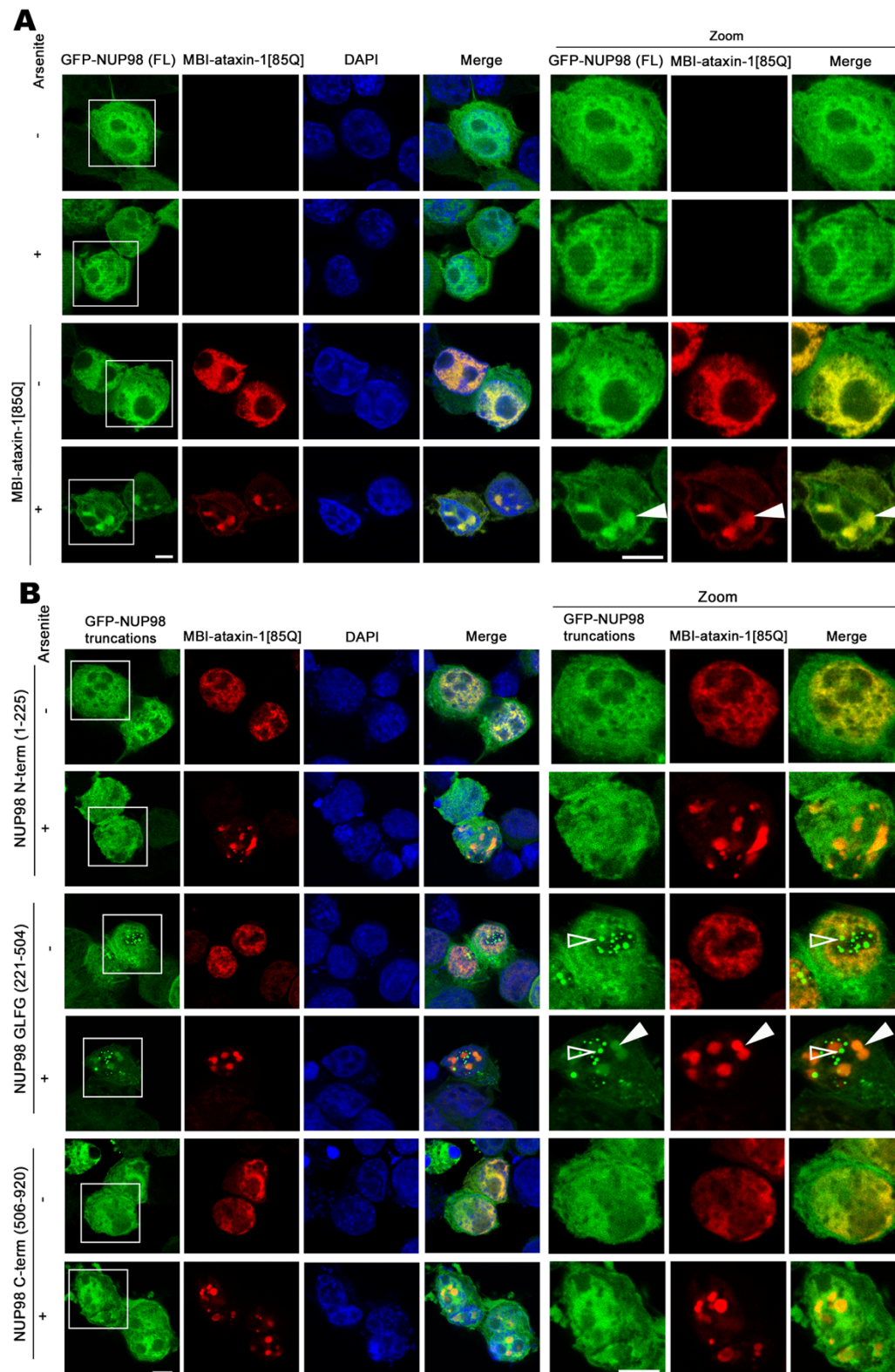


Fig. S1

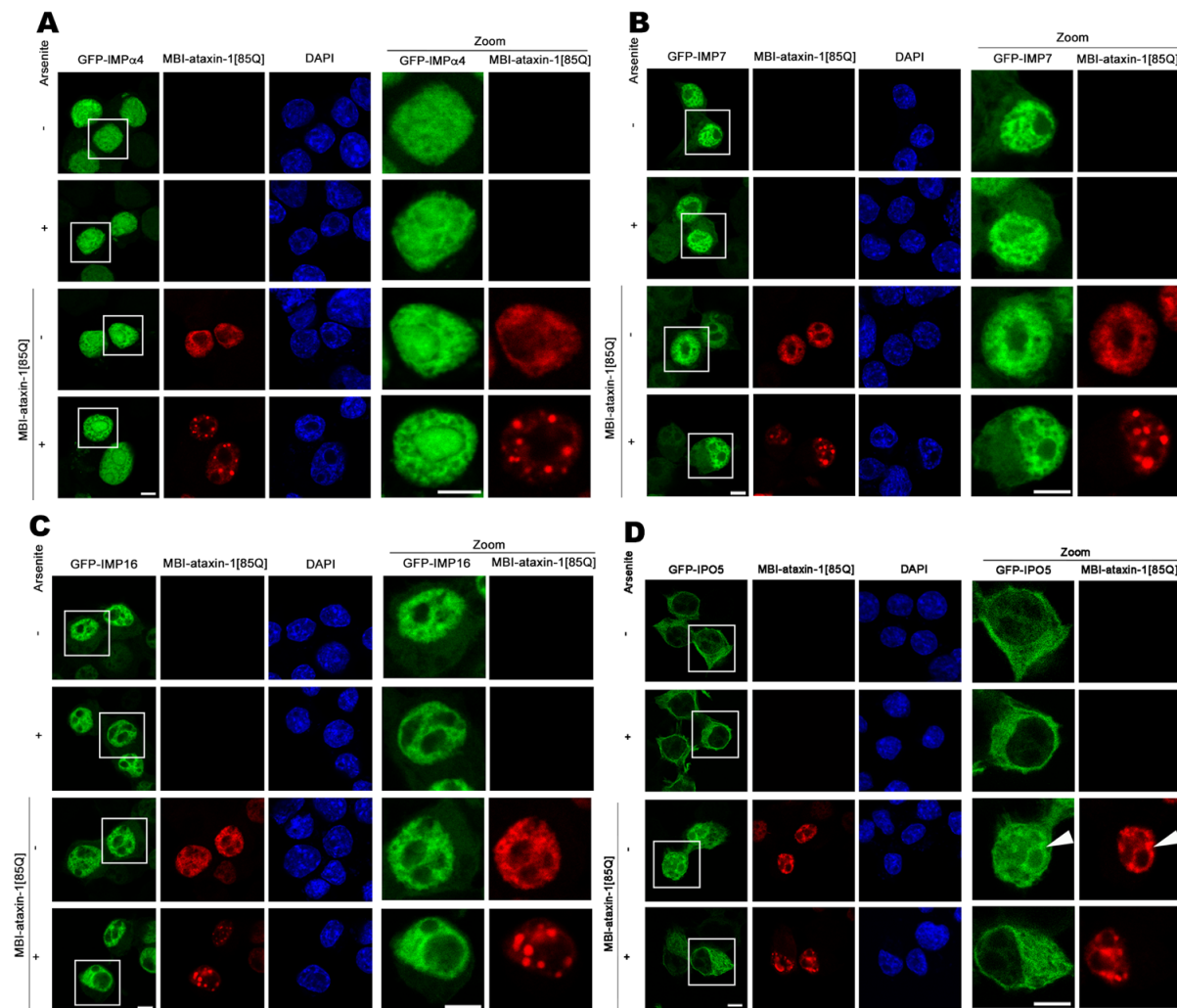


Fig. S2

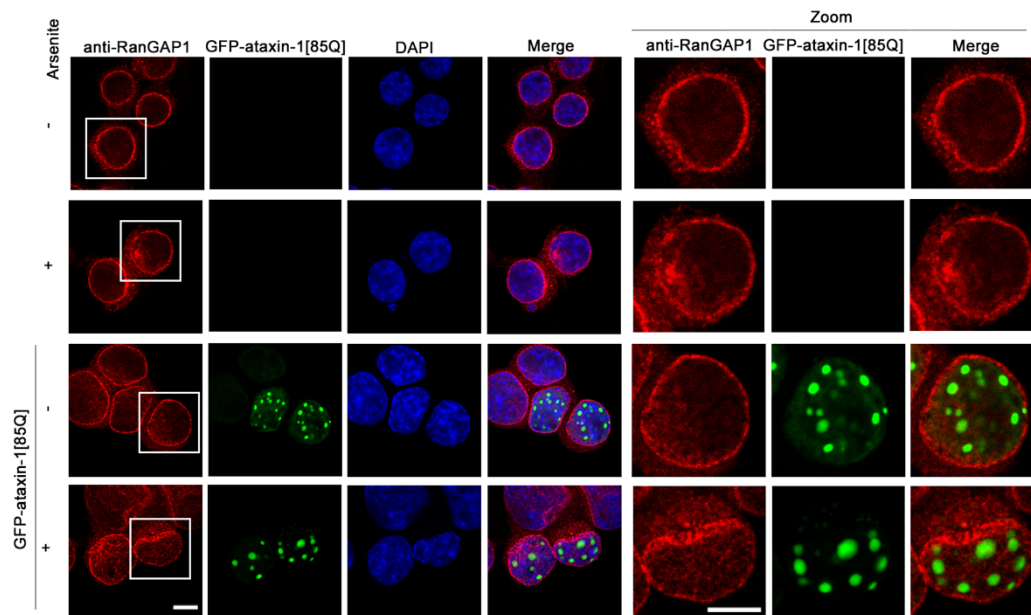


Fig. S3

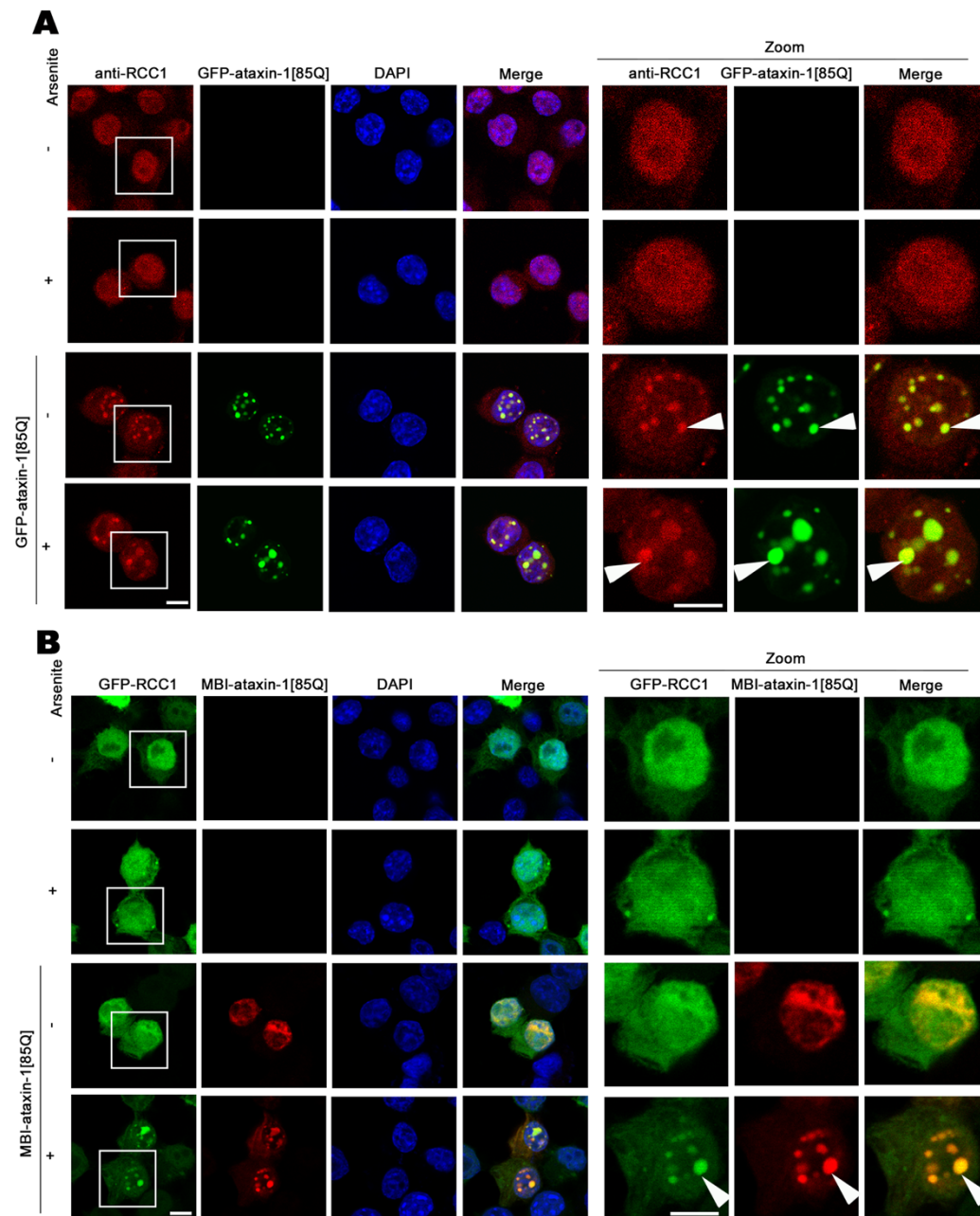


Fig. S4

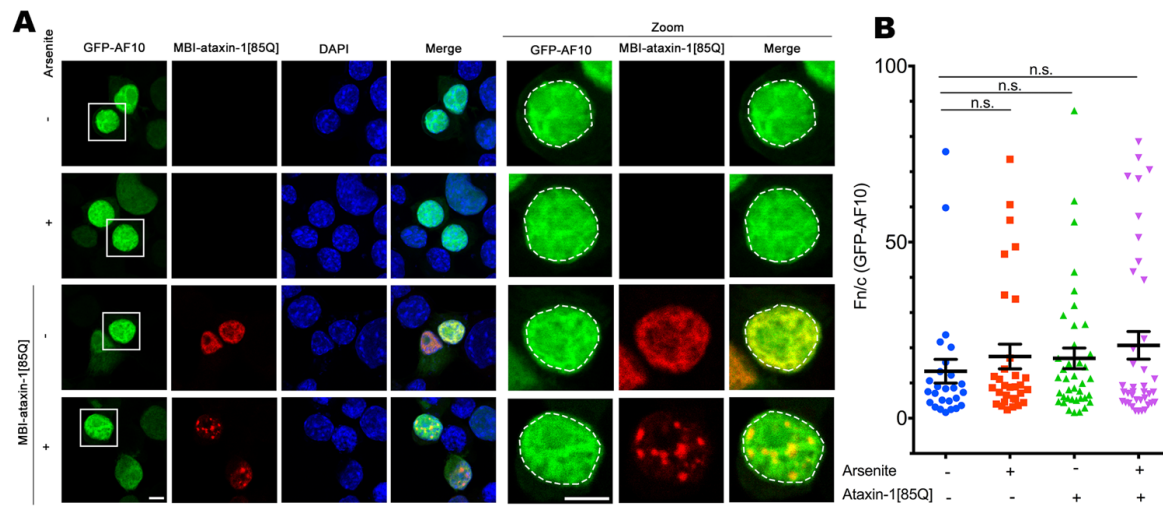


Fig. S5

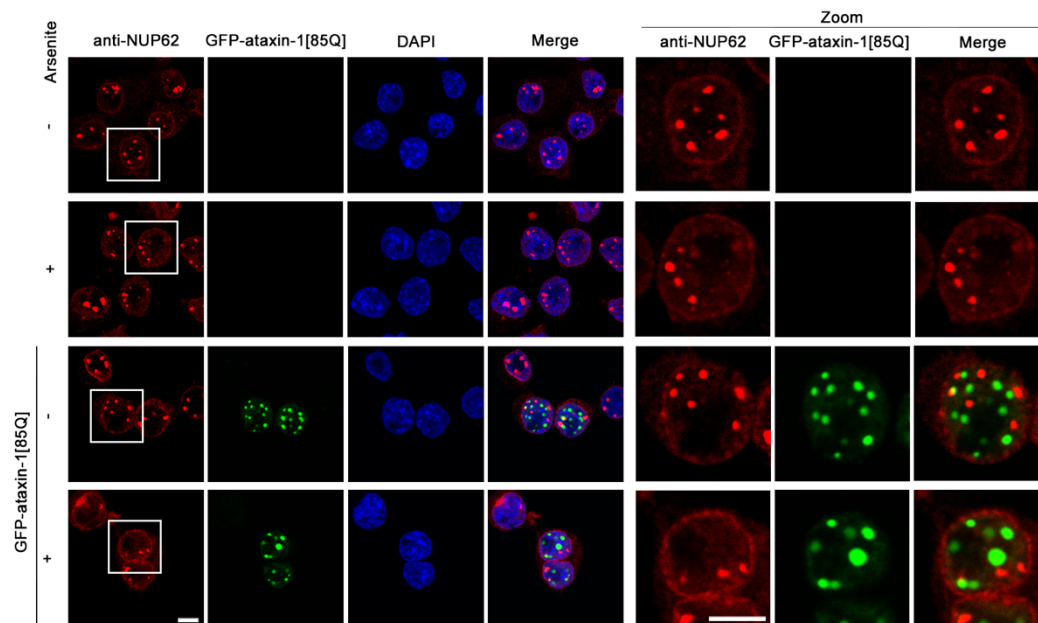


Fig. S6

